Ultrasound in Med. & Biol., Vol. 44, No. 8, pp. 1727–1741, 2018

0301-5629/$ - see front matter

https://doi.org/10.1016/j.ultrasmedbio.2018.03.017

● *Original Contribution*

ACCURACY AND PRECISION OF A PLANE WAVE VECTOR FLOW IMAGING METHOD IN THE HEALTHY CAROTID ARTERY

Jonas Jensen,* Carlos Armando Villagómez Hoyos,* Marie Sand Traberg,* Jacob Bjerring Olesen,* Borislav Gueorguiev Tomov,* Ramin Moshavegh,* Simon Holbek,* Matthias Bo Stuart,* Caroline Ewertsen,† Kristoffer Lindskov Hansen,† Carsten Thomsen,† Michael Bachmann Nielsen,† and Jørgen Arendt Jensen*

* Center for Fast Ultrasound Imaging, Department of Electrical Engineering, Technical University of Denmark, Lyngby, Denmark; and † Department of Radiology, Copenhagen University Hospital, Copenhagen, Denmark

(*Received* 28 *April* 2017; *revised* 4 *March* 2018; *in final form* 19 *March* 2018)

Abstract—The objective of the study described here was to investigate the accuracy and precision of a plane wave 2-D vector flow imaging (VFI) method in laminar and complex blood flow conditions in the healthy carotid artery. The approach was to study (i) the accuracy for complex flow by comparing the velocity field from a computational fluid dynamics (CFD) simulation to VFI estimates obtained from the scan of an anthropomorphic flow phantom and from an *in vivo* scan; (ii) the accuracy for laminar unidirectional flow *in vivo* by comparing peak systolic velocities from VFI with magnetic resonance angiography (MRA); (iii) the precision of VFI estimation *in vivo* at several evaluation points in the vessels. The carotid artery at the bifurcation was scanned using both fast plane wave ultrasound and MRA in 10 healthy volunteers. The MRA geometry acquired from one of the volunteers was used to fabricate an anthropomorphic flow phantom, which was also scanned using the fast plane wave sequence. The same geometry was used in a CFD simulation to calculate the velocity field. Results indicated that similar flow patterns and vortices were estimated with CFD and VFI in the phantom for the carotid bifurcation. The root-mean-square difference between CFD and VFI was within 0.12 m/s for velocity estimates in the common carotid artery and the internal branch. The root-mean-square difference was 0.17 m/s in the external branch. For the 10 volunteers, the mean difference between VFI and MRA was –0.17 m/s for peak systolic velocities of laminar flow *in vivo*. The precision *in vivo* was calculated as the mean standard deviation (SD) of estimates aligned to the heart cycle and was highest in the center of the common carotid artery (SD = 3.6% for velocity magnitudes and 4.5° for angles) and lowest in the external branch and for vortices (SD = 10.2% for velocity magnitudes and 39° for angles). The results indicate that plane wave VFI measures flow precisely and that estimates are in good agreement with a CFD simulation and MRA. (E-mail: jaj@elektro.dtu.dk)

Key Words: **Blood velocity estimation, Vector flow imaging, Plane wave imaging, Complex flow, Carotid artery.**

INTRODUCTION

Atherosclerosis is a precursor to many cardiovascular diseases and the leading cause of death worldwide (Naghavi et al. 2003). Blood clots originating from the carotid arteries are especially important, as they may be responsible for stroke (Bamford et al. 1991). Assessment of the carotid artery is therefore of particular interest. Magnetic resonance angiography (MRA) and ultrasound (US) are non-invasive techniques for imaging flow in blood vessels. MRA is a time-consuming and expensive technique with a spatial resolution of, typically, 1 mm and a frame rate of 50 Hz. Depending on the manufacturer of the MRA scanner, the scan time can lapse from 5 to 15 min while it acquires a few hundred heart cycles, which are then combined (Lotz et al. 2002). US imaging is a relatively inexpensive technique, which is used in daily clinical practice and provides blood flow velocities in real time with sub-millimeter resolution. B-Mode and color flow imaging are used for orientation and flow visualization, and quantitative parameters are calculated from the spectrogram.

Although peak systolic velocity (PSV), end-diastolic velocity, resistive index and volume flow are typical and

Address correspondence to: Jonas Jensen, Technical University of Denmark, Ørsteds Plads, Building 349, DK-2800 Lyngby, Denmark. E-mail: jaj@elektro.dtu.dk

widely used quantitative measures for characterizing the flow, there are several limitations. The velocity estimate is only found along the US beam, that is, in the axial direction, and has to be corrected for the beam-to-flow angle. This is often performed manually by the examiner and is largely inter-/intra-operator dependent, and the estimates are prone to large errors (Corriveau and Johnston 2004; Stewart 2001). The correction only works when laminar and uni-directional flow is parallel to the vessel (Kruskal et al. 2004). However, most vessels are curved and have branches, creating complex blood flow patterns. For pulsating flow, the flow angle may also change during the cardiac cycle. Complex flow is multi-directional and can be characterized as a $> 90°$ change in flow angles within an area (Pedersen et al. 2014). As opposed to turbulent flow, complex flow patterns are repeatable from heart cycle to heart cycle, as for many vortices and recirculation zones. The spatially and temporally varying flow angles for complex flow limit the use of spectral Doppler, and the placement of the range gate for velocity estimation at a single location is operator dependent (Lui et al. 2005).

The development in 2-D vector flow imaging (VFI) has provided velocity estimation methods without the need for angle correction. Cross-beam methods (Dunmire et al. 2000; Fox 1978), speckle tracking (Trahey et al. 1987), transverse oscillation (TO) (Anderson 1998; Jensen and Munk 1998), directional beamforming (DB) (Jensen 2003) and spectral-based methods (Newhouse et al. 1987; Tortoli et al. 2006) have been suggested for finding the 2-D velocity vector. The combination of VFI and high-frame-rate techniques such as synthetic aperture (Nikolov and Jensen 2003) and plane wave imaging (Bercoff et al. 2011; Ekroll et al. 2013; Lenge et al. 2015; Udesen et al. 2008; Yiu et al. 2014) has further improved performance of the methods. The advantages are that quantitative velocity estimates can be obtained everywhere in the image at hundreds to thousands of frames per second, and no angle correction is needed. VFI provides a more complete picture of flow patterns, which are often transient and complex (Hansen et al. 2009a). Data are available continuously for plane wave and synthetic aperture imaging, which improve the precision of the estimates because averaging can be performed over a number of emissions without sacrificing frame rate (Nikolov and Jensen 2003).

Any VFI method must yield precise and accurate velocity estimates for both laminar uni-directional flow and complex flow when measured *in vivo*. This is especially important for quantitative measurements derived from any spatial estimation point in the image. The accuracy of VFI methods has previously been investigated for uni-directional flow in the common carotid artery by comparing PSV and volume flow estimates with independent methods such as spectral Doppler and MRA (Ekroll et al. 2014; Hansen et al. 2009b; Tortoli et al. 2015). However, two challenges arise for further investigation of accuracy and precision: (i) Compared with VFI methods, neither spectral Doppler nor MRA has sufficiently high spatial and temporal resolution to accurately capture complex flow patterns *in vivo*. (ii) To evaluate the precision of a method in terms of repeatability of estimates, acquisition of data on at least two to three heartbeats is required, but this generates more transducer element data than most scanners can store when using high-frame-rate imaging.

In relation to (i), one approach to investigation of complex flow is the use of computational fluid dynamics (CFD) simulations of the velocity field within a vessel geometry. CFD simulations have been extensively used to study the flow fields existing in the carotid arteries (Cebral et al. 2002; Steinman et al. 2000) and can be employed as an independent method for comparison with ultrasound. Although an *in vivo* scan represents the most realistic data acquisition for VFI, there is no ground truth, which makes a comparison between a CFD velocity field and VFI challenging. A VFI phantom measurement may be employed to establish a link between US simulations and *in vivo* measurements, as several flow conditions can be mimicked in the phantom and taken into account in the CFD modeling. This allows a more quantitative comparison between CFD and VFI. Flow phantoms can be made from anthropomorphic geometries using novel fabrication processes, whereby complex flow patterns in a realistic vessel geometry and environment may be measured using VFI (Lai et al. 2013).

In relation to (ii), all element data can be stored in scans for up to 10 s using the experimental scanner SARUS, which can store data up to 96 GB (Jensen et al. 2013). Thereby, the precision of flow estimation methods can be evaluated from several heartbeats.

The method for VFI used in the study described here is based on plane wave imaging and a combination of TO and DB (Jensen et al. 2017). It has previously been validated in simulations of straight vessels and a carotid bifurcation model, and a single *in vivo* scan has also been presented (Jensen et al. 2017).

The objective of our study was to investigate the accuracy and precision of the method *in vivo* in the carotid artery of 10 healthy volunteers. The approach used was to:

- Perform a quantitative comparison of VFI estimates measured in an anthropomorphic phantom with a CFD velocity field to study the accuracy under complex flow conditions,
- Perform a qualitative comparison of the VFI velocity field obtained from an *in vivo* scan with a CFD velocity field,
- Study the accuracy *in vivo* for laminar uni-directional flow by comparing VFI estimates with spectral Doppler and MRA, and

- Evaluate the precision *in vivo* by calculating the repeatability of the VFI estimates at several estimation points in the vessels.

Flow measurements were performed in the carotid artery encompassing the bifurcation in healthy volunteers. Flow in the common carotid artery (CCA) is expected to be laminar uni-directional, whereas complex flow patterns occur in the carotid bulb (Pedersen et al. 2014). These parts of the carotid artery were used to study the VFI method.

EXPERIMENTAL METHODS

Ten healthy volunteers with no history of cardiac, vascular or neurologic disease were recruited (8 males and 2 females; mean body mass index: 24 kg/m^2; median age: 31 y, range: 25–52 y). The volunteers participated after submitting informed consent, and the study was approved by the National Committee on Biomedical Research Ethics (Protocol No. H-1-2014-fsp-072). Data acquisition for each volunteer spanned 1 day. The *in vivo* VFI scan was conducted during a session in the morning, and the MRA scan was performed in the afternoon. One radiologist, either C.E. or K.L.H., performed the US VFI scan, and both performed the MRA scan. All measurements were performed with the volunteer in a supine position. Volunteers rested in this position for at least 10 min before each scan.

In vivo VFI scans and processing

Prior to the plane wave VFI scans, a scan of the right CCA in long-axis view was performed 2–3 cm before the bifurcation using a linear array transducer (BK 8L2, BK Ultrasound, Herlev, Denmark) and a commercial scanner (BK3000, BK Ultrasound). A spectral Doppler measurement was made, and a 15-s cine loop with the spectrogram was recorded. The spectral Doppler beam was steered to keep the beam-to-flow angle <60° (mean beam-to-flow angle: 45.7°, range: 42°–56°). The plane wave VFI scans were then performed using the same transducer type, which was connected to the experimental US scanner SARUS (Jensen et al. 2013). A duplex sequence consisting of both flow and B-mode emissions was employed (Jensen et al. 2017). Transducer and processing parameters are listed in Table 1. Each of the two scans was recorded separately: (i) a longitudinal scan at the right CCA 2–3 cm before the bifurcation, and (ii) a longitudinal scan at the carotid bulb with the best possible view of the bifurcation. Transducer element data were acquired for a total of 10 s for each scan and were stored for further processing.

Beamforming was performed offline, and an energy-based filter with manual threshold was used for echo canceling of beamformed data (Villagomez-Hoyos et al. 2017). The energy-based cutoff filter was used instead of a conventional frequency cutoff filter to separate better the blood signal from the tissue signal of moving vessel walls. The energy-based filter used the amplitude characteristics of blood and tissue, and tissue components were attenuated by limiting the amplitude of the tissue velocity spectrum to a cutoff threshold. The threshold was determined by using data from one of the volunteers as a training set, and the same threshold was then applied to all scans of volunteers. For details on the filter and its impact on the performance of the velocity estimates, the reader is referred to Villagomez-Hoyos et al. (2017).

Table 1. Transducer and acquisition parameters

Parameter	Value
Number of elements	192
Transducer center frequency f_0	4.1 MHz
Cycles in emitted pulse	1.5 (flow), 1 (B-mode)
Transmit apodization	Tukey (weight 0.5)
Pulse repetition frequency f_{prf}	10 kHz
Max steering angle	15° (flow), 20° (B-mode)
Number of plane waves	3 (flow), 21 (B-mode)
Receive apodization	Tukey (weight 0.5)
Desired TO wavelength	2 mm
DB angle spacing	2°–10°
Number of HRI/estimate	32
Frame rate (velocity estimation)	300 Hz

DB = directional beamforming; HRI = high resolution image; TO = transverse oscillation.

A two-step procedure was employed for vector velocity estimation: First, the TO method was used to find an initial flow angle θ calculated from the axial, v_z, and lateral, v_x, velocity components. The transverse oscillation was created by applying a Gaussian filter on the beamformed images in the Fourier domain (Salles et al. 2015). Second, three directional lines were beamformed around the TO angle θ at each estimation point in the image to find a refined angle estimate $\hat{\theta}$. The refined angle was calculated from the angle yielding the largest normalized cross-correlation estimate based on the three directional lines. The velocity magnitude was estimated along the flow direction $\hat{\theta}$ using a cross-correlation estimator. For further details on the vector velocity method, the reader is referred to Jensen et al. (2017).

Intensities of the applied plane wave sequence were as follows: mechanical index (MI) = 1.25, and derated spatial-peak temporal average intensity $\left(I_{\text{spta.3}}\right) = 267\ \text{mW/cm}^2$, which were within the U.S. Food and Drug Administration (FDA) limits (FDA 2008). Transducer surface temperature rise was measured to 18.6 °C in still air and 6.3 °C when attached to a phantom. The values were below the FDA limits of 27 °C and 10 °C, respectively.

MRA scans and processing

A 1.5-T whole-body scanner (Magnetom Avanto, Siemens, Erlangen, Germany) was used in combination

with a head and a neck matrix coil. A time-of-flight sequence was performed as a localizer for the carotid artery. A cross-sectional plane of the CCA was selected 2–3 cm before the bifurcation by consulting the anatomical image. Through-plane velocities were estimated within the plane by using a retrospective electrocardiogram-gated phase contrast sequence. The sequence had a repetition time of 42 ms, echo time of 3 ms, flip angle of 20°, pixel resolution of 1.1 × 1.1 mm and slice thickness of 5 mm. Estimates were retrieved from 210 heartbeats, and the total number of phases per heartbeat was 50. The phase contrast sequence was repeated three times to obtain three independent estimates of velocities within the same plane. Anatomical images were also acquired for a volume covering the common carotid artery and carotid bulb. The acquisition was made in parallel to the applied flow sequence, and the resolution was the same as for the flow data.

The stored MRA DICOM files contained anatomical and through-plane velocity estimates in 50 frames during a cardiac cycle. Each velocity data set was processed offline by adding the 50 frames to create a combined anatomical intensity map. Vessel regions were segmented by creating a binary image based on the intensity map and applying a manually selected threshold. The threshold was adjusted for each data set and each volunteer. Potential vessels were detected by applying morphological operations on the binary image (Holbek et al. 2017). A vessel region containing the right CCA was selected manually, and flow estimates within this region were detected and stored for further analysis of MRA flow.

A 3-D geometry representing the carotid artery of one of the volunteers was used to produce a CFD model and a flow phantom with a geometry similar to that of the scanned vessel. This was achieved by concatenating the collected MRA images in ScanIP (Simpleware Ltd., Exeter, UK) and marking the vessel region by creating a binary mask by applying a threshold on the anatomical intensity images. The segmented flow volume was imported into SolidWorks (Education edition, Dassault Systèmes SolidWorks Corp., Vélizy, France), where smoothing of the geometry was performed prior to flow phantom fabrication and CFD simulation.

Flow phantom fabrication and scan

An anthropomorphic flow phantom matching the flow domain of the original scanned vessel was fabricated using stereolithography, a technique described by Lai et al. (2013). A Leapfrog Creatr HS XL printer (Leapfrog BV, Alphen aan den Rijn, Netherlands) with a depth–width resolution of 17 μm and a resolution in height of 20 μm was used to print the drafted vessel. The 3-D printed geometry constituted a temporary core in the wall-less phantom. The core was fixated in a container and cast in polyvinyl alcohol (PVA) cryogel to obtain a surrounding medium, which mimicked the properties of human tissue. The PVA cryogel contained 10% PVA, 1% silicon dioxide, 0.3% potassium sorbate and 83.7% distilled water. The elastic properties of the cast material were controlled by varying the number of freeze–thaw cycles. Three freeze–thaw cycles were used, where each half-cycle lasted 24 h, the freeze settings were −20 ± 0.5 °C and the thaw settings were 4 ± 0.5 °C. The core was removed manually after the completion of three cycles (total duration = 144 h). The resulting phantom was core-less with a fluid domain identical to that of the original scanned vessel.

The anthropomorphic phantom was connected to a closed-loop flow system (CompuFlow 1000, Shelley Medical Imaging Technologies, Toronto, ON, Canada) that circulated a blood-mimicking fluid (BMF-US, Shelley Medical Imaging Technologies, Toronto, ON, Canada) with a viscosity of 4.1×10^{-3} Pa·s and a density of 1030 kg/m^3. The CompuFlow system was set to generate a standard carotid artery waveform to mimic the flow in this artery. The peak volume flow was 15 mL/s, and the cardiac period was 0.84 s, which were within representative physiological ranges. The transducer was placed on the phantom and the scan plane was longitudinal to the bifurcation. Data on 10-s recordings were acquired with the SARUS scanner using the same sequence and parameters used for the *in vivo* scans. The echo-cancel filter and vector velocity estimation were also the same as for the *in vivo* scans.

CFD model

Flow simulation in the CFD model was governed by solving the Navier–Stokes equations. The properties of the emulated fluid matched those of the blood-mimicking fluid used for the phantom study and those of the blood in the *in vivo* study, respectively. It was assumed that the fluid was Newtonian, entrance effects were discarded, the vessel was rigid and the flow had reached a steady state of pulsation. An outlet pressure of 0 Pa was set for the two exit branches representing the internal carotid artery (ICA) and external carotid artery (ECA), and a no-slip condition was set at the walls of the flow domain.

The inlet condition was constructed using the Womersley–Evans model (Evans 1982; Womersley 1955). The individual components of a measured mean spatial velocity curve were determined by Fourier decomposition. Thereafter, superposition of the first 10 harmonics provided a smooth spatial velocity variation. It was used to reconstruct the velocity profile in both time and space using the Womersley–Evans model. Two mean spatial velocity curves were used for the two CFD simulations: one used the measured plane wave VFI data at a point in the

CCA of the flow phantom, and the other used the through-plane velocity information from the MRA scan to mimic the *in vivo* flow conditions.

All CFD simulations were run six consecutive times corresponding to six cardiac cycles. This was done to ensure a stable solution. The simulations were carried out in Comsol Multiphysics (Version 5.2a, Comsol AB, Stockholm, Sweden). On average, the computation time for the six consecutive cycles was 3 h using a standard PC (Dell Precision Tower 5810, Intel(R) Xeon(R), 20 cores). The mesh consisted of 437,444 elements with an average element quality of 0.621 (1 = high quality, 0 = poor quality).

METHODS FOR EVALUATION

Comparison between phantom VFI and CFD

Comparison between the flow field of the CFD simulation and phantom VFI measurement required that the geometries be aligned. The VFI measurement provided velocities in a plane of the 3-D geometrical phantom, and the CFD model provided velocities in the full 3-D volume of the phantom. The vessel was manually segmented on a B-mode image from the VFI to provide a geometry of the vessel in the scanned plane. The CFD geometry was then rotated and translated to the coordinate system of the VFI plane to align the two geometries. This was performed manually by visual inspection of the geometries. The applied translation and rotation were also used to convert the CFD velocities into velocity components in the coordinate system corresponding to the VFI. CFD velocities were interpolated to the same locations as in the VFI, and an inter-frame linear interpolation was used to process the same time instances.

Thereby, quantitative comparisons of velocities acquired from CFD and VFI were made. This included the vorticity

$$\omega = \nabla \times \vec{v} = \left(\frac{\partial v_z}{\partial x} - \frac{\partial v_x}{\partial z} \right) \quad (1)$$

where ∇ is the nabla operator. The total vorticity was calculated for an area covering a part of a recirculation zone. Vorticity has previously been used to characterize flow rotations and vortices in the carotid bulb and the ascending aorta (Hansen et al. 2017; Pedersen et al. 2011).

Comparison between VFI in vivo and CFD

The comparison between the flow field of the CFD simulation and the VFI *in vivo* scan was also made after manual alignment. Selected frames at peak systole and within systolic deceleration were used in a qualitative comparison.

Comparison between VFI, MRA and spectral Doppler

The PSV in scans of laminar flow in the CCA of each volunteer was compared for plane wave VFI, spectral Doppler and MRA. For the plane wave VFI of the CCA, PSVs were estimated at every velocity estimation point within the segmented vessel and for each cardiac cycle. The estimation point with the maximum PSV was detected, and the mean and standard deviation (SD) of the PSVs during the 10-s scan sequence were calculated. For the spectral Doppler scans, the PSV estimated by the scanner was read from the 15-s cine loop for each volunteer. For the MRA scans, mean velocities were provided throughout one cardiac cycle because of the combination of several cardiac cycles with ECG gating. PSVs was for each of the three MRA data sets were determined for each volunteer and averaged. The PSV for plane wave VFI was compared with those for MRA and spectral Doppler using Bland–Altman plots and linear regression. A multiple comparison was performed using Tukey's test and a significance level of 0.05.

Precision of VFI in vivo

The VFI and B-mode data sets from the *in vivo* scans were imported into an in-house developed MATLAB-based visualization tool. Vector velocities were laid over B-mode images, and a color wheel map represented the velocity magnitude and direction of the blood flow. A video of the full 10-s acquisition was played and could be stopped at any frame.

A medical doctor (K.L.H.) with 10 years of experience in VFI evaluated each of the 2×10 scans by selecting evaluation points according to a defined procedure for longitudinal scans of the CCA (one point in the center of the vessel and one point near the upper vessel wall) and longitudinal scans at the carotid bulb (a point in the center of a part of the CCA, near the upper vessel wall of the CCA, in the ECA, and in the ICA).

A box encompassing a vortex in the carotid bulb was also marked for each scan. It was tried to encompass as much of the vortex without including additional flow regions. If any of the vessels or a vortex were not visible on the scans, an evaluation point/box was not selected.

For each evaluation point selected, the program automatically calculated the mean cardiac cycle based on the velocity estimates by using the autocorrelation function. A 10-s scan sequence typically consisted of 7–11 cardiac cycles. The velocity magnitude and angle estimates at the evaluation points and the vorticity calculated inside the box using eqn (1) were coherently aligned according to the cardiac period. Ninety percent of the mean cardiac period was used for the alignment (15% before and 75% after the peak systolic value), because small deviations in the heart rate were found throughout the 10-s scan period. The standard deviation $\sigma(t)$ at time t in the cardiac cycle was

calculated among the aligned estimates. The mean SD for each point was then

$$\mathrm{SD} = \sqrt{\frac{1}{N_\mathrm{f}} \sum_{t=1}^{N_\mathrm{f}} \sigma(t)^2} \qquad (2)$$

where N_f is the number of frames encompassing a cardiac cycle. For the mean SD of the velocity magnitude and the vorticity, eqn (2) was calculated relative to the peak value. The median value of the mean SD among the 10 volunteers was also calculated.

RESULTS

Comparison of phantom VFI and CFD

The VFI scan plane aligned with the CFD geometry is illustrated in Figure 1. The width of the scan plane in the elevation direction was set according to the elevational width of the ultrasound beam at the elevation focus of the probe. The segmented vessel from the VFI fitted generally well within the 3-D mesh of the CFD simulation. There was, however, about 0.5 to 1 mm of misalignment in the ECA and at the outlet of the ICA. A qualitative comparison between velocity fields obtained from plane wave VFI and the CFD simulation is presented below, and a quantitative comparison follows hereafter.

Frames from two phases of the cardiac cycle are illustrated in Figures 2 and 3: during peak systole (0.16 s) and systolic deceleration (0.32 s). Estimates are shown for the CFD simulation and for the first cardiac cycle in the VFI scan. During peak systole, the VFI velocity fields in the CCA and ECA had patterns similar to that of the CFD simulation. The velocity magnitudes were at the same levels, and the arrows pointed in the same direction. For the ICA, the largest velocities were obtained close to the inner vessel wall of the ICA, and a vortex appeared near the upper wall. The vortex in the ICA was moved slightly further up in the VFI measurement and was merely an area of very low velocities rather than a well-defined vortex. It also affected the blood flow pattern downstream. During systolic deceleration (Fig. 3), both the CFD and VFI had a large vortex or recirculation zone, which extended from the CCA into the ICA. There were small differences in the extent of the recirculation for CFD and VFI, but similar flow patterns were provided. A jet of streamlined forward flow was found close to the inner vessel wall of the ICA in the CFD and VFI. A smaller vortex in the ECA was also visible in the VFI; however, this vortex was not visible in the CFD. Furthermore, the speed of flow in the ECA and the CCA was lower in the VFI than in the CFD.

Quantitative comparison of CFD and VFI velocity estimates is illustrated in Figures 4 and 5. Velocity estimates at all spatial positions for the frames at peak systole and systolic deceleration were used. Colors encode estimates from the CCA (*blue*), ICA (*red*) and ECA (*yellow*). The root-mean-square (RMS) difference between the measured VFI estimates and CFD was calculated for the three parts of the bulb and was in the range 0.023 to 0.047 m/s for v_z at peak systole and systolic deceleration. For v_x at peak systole (Fig. 4), the RMS difference was highest in the ECA (0.16 m/s) as the estimates with VFI were measured higher than those with CFD. Velocity estimates in the ICA covered a large range from 0.1 to 0.5 m/s as

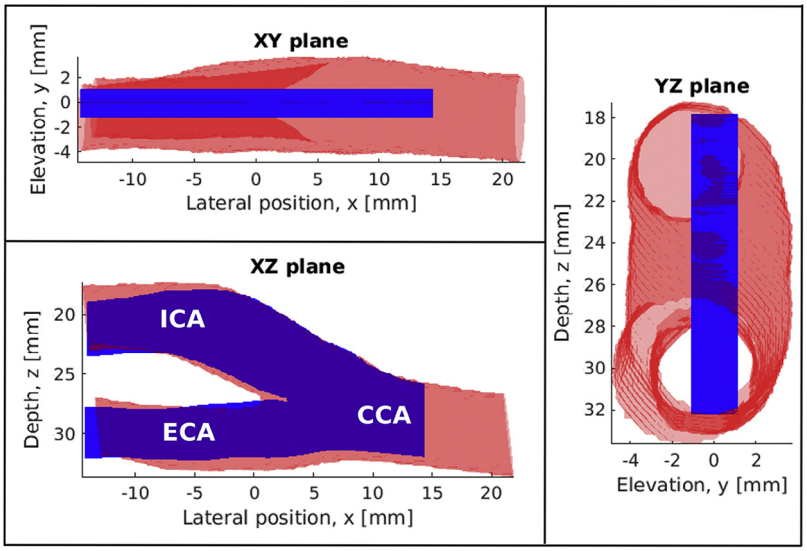

Fig. 1. Alignment of the computational fluid dynamics vessel geometry (*red*) to the vector flow imaging scan plane (*blue*) in the phantom scan. The elevation of the ultrasound beam is indicated by the width of the *blue rectangle* in the XY and YZ planes. CCA = common carotid artery; ECA = external carotid artery; ICA = internal carotid artery.

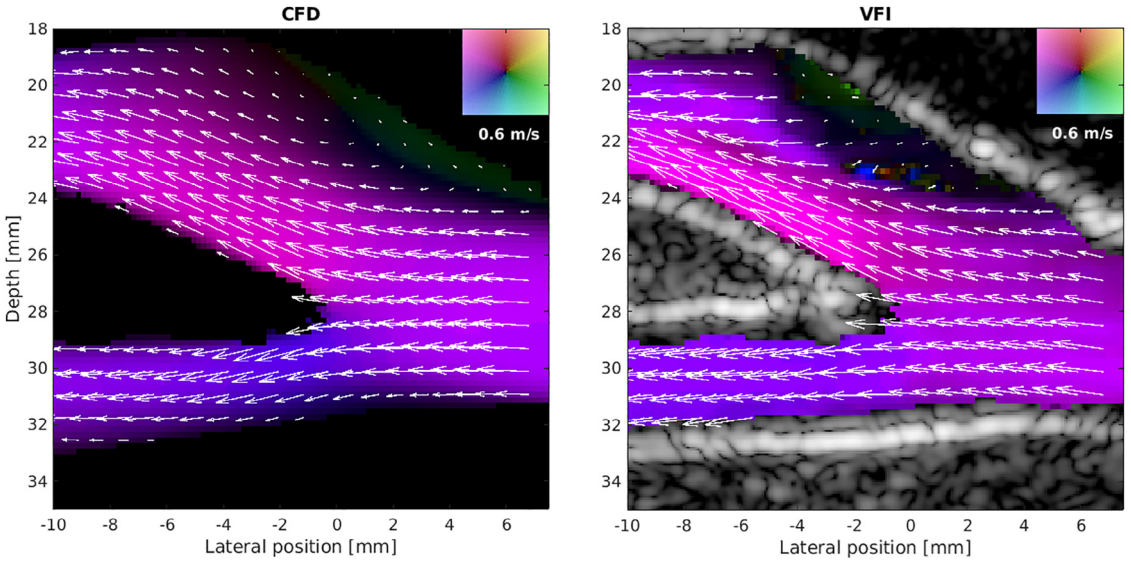

Fig. 2. Velocity estimates from the CFD simulation (left) and VFI scan of phantom (right). The frame is from the peak systolic phase ($t = 0.16$ s). CFD = computational fluid dynamics; VFI = vector flow imaging.

confirmed by the vortex and high-flow speeds in Figure 2. The RMS difference was 0.11 m/s. For v_x at systolic deceleration (Fig. 5), VFI yielded generally lower velocities compared with CFD. The RMS difference was largest in the CCA and ECA (0.17 m/s and 0.14 m/s, respectively), whereas it was 0.09 m/s in the ICA.

The temporal evolution of the flow patterns is evident in a video sequence from the full acquisition (Supplementary Video S1, online only). It revealed that a vortex quickly built up and disappeared in the ICA during systole for the VFI scan, before a larger vortex appeared at the same location and was fully developed during systolic deceleration. For the CFD simulation, a single vortex in the ICA built up during late systole and was fully developed in systolic deceleration.

The temporal changes in the flow field can also be observed in Figure 6. In Figure 6(a), the velocity magnitude is plotted as a function of time for an estimation point in the CCA, which is also indicated by the *white circle* in Figure 3. The shape of the velocity magnitude profile for VFI in Figure 6(a) was similar to that for CFD. However, velocities were estimated lower for VFI than for

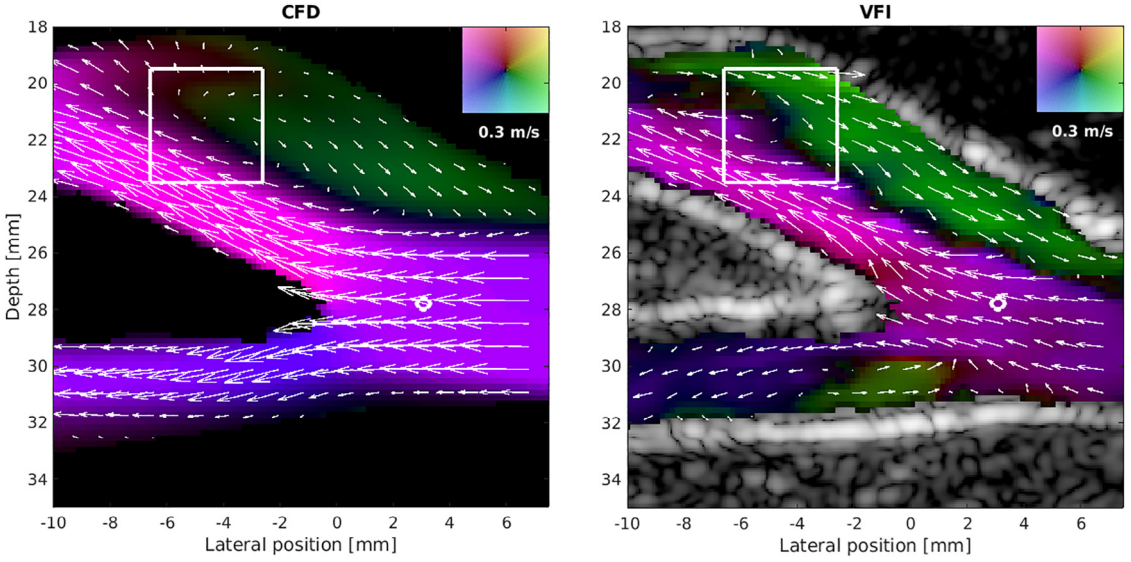

Fig. 3. Velocity estimates from CFD simulation (left) and VFI scan of phantom (right). The frame is within the systolic deceleration ($t = 0.32$ s). The velocity magnitude sampled at the *white circle* is depicted in Figure 6(a), and the vorticity in the *white box,* in Figure 6(b). CFD = computational fluid dynamics; VFI = vector flow imaging.

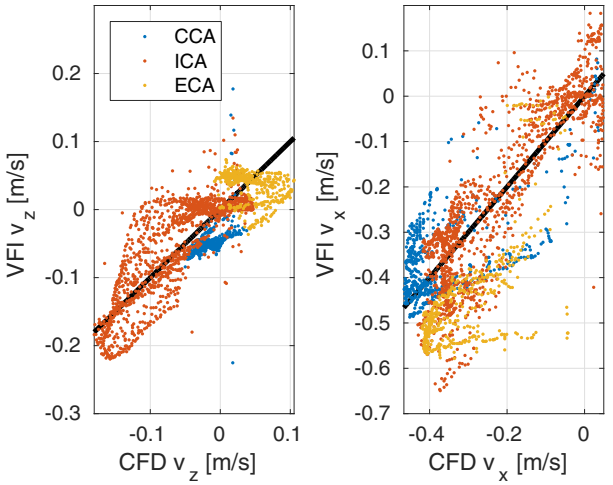

Fig. 4. Scatterplots of measured vector flow imaging estimates versus simulated computational fluid dynamics estimates at peak systole ($t = 0.16$ s). Axial velocity estimates v_z (left) and lateral velocity estimates v_x (right). CCA = common carotid artery; CFD = computational fluid dynamics; ECA = external carotid artery; ICA = internal carotid artery; VFI = vector flow imaging.

CFD, especially during diastole, which resulted in a mean difference between CFD and VFI of −12.7%. For the vorticity calculated in the ICA, the evolution of vortices during two points in Supplementary Video S1 was also confirmed: the vorticity had two maxima (at 0.14 and 0.3 s) in the VFI measurements, whereas a single vortex built up after 0.15 s in the CFD simulation. It was suspected that vessel wall movement in the phantom might be a reason for the difference in flow patterns between VFI and

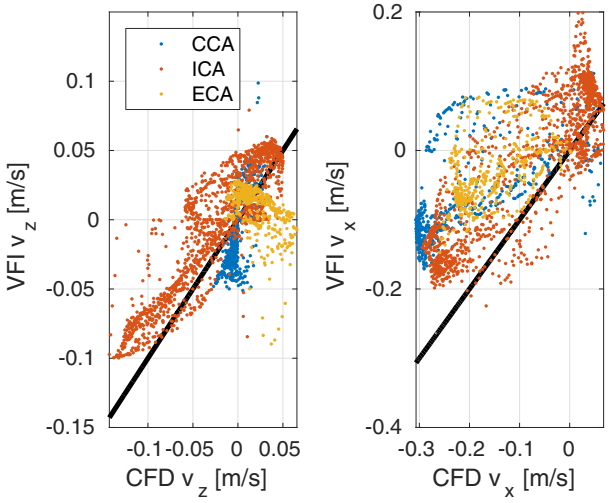

Fig. 5. Scatterplots of measured VFI estimates versus simulated CFD estimates during systolic deceleration ($t = 0.32$ s). Left: Axial velocity estimates v_z. Right: Lateral velocity estimates v_x. CCA = common carotid artery; CFD = computational fluid dynamics; ECA = external carotid artery; ICA = internal carotid artery; VFI = vector flow imaging.

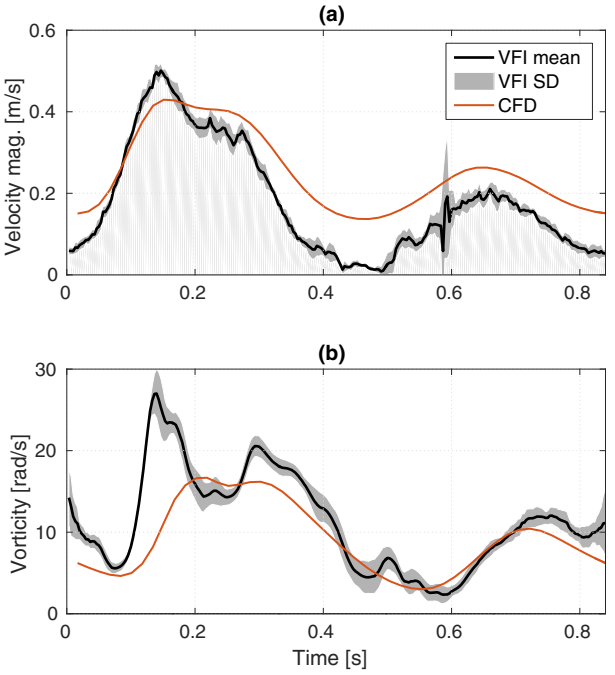

Fig. 6. (a) Velocity magnitude is plotted as a function of time during the cardiac cycle for an estimation point in the common carotid artery. (b) Vorticity as a function of time inside a box in the internal carotid artery. The estimation point in (a) is also marked by a *white circle* in Figure 3, and the vortex, by a *white square*. *Black graphs* are the mean VFI estimates, the *gray area* represents the standard deviations of VFI estimates and the *red graphs* are CFD estimates. CFD = computational fluid dynamics; VFI = vector flow imaging.

CFD simulation during systole. The vessel wall movement was therefore quantified by estimating tissue velocities from the flow data and disabling the echo-canceling filter. The largest tissue velocities for a point on the proximal vessel wall were ±2 mm/s and were attained at 0.1 and 0.2 s during systole. A few milliseconds later, vortices appeared in the ICA in the phantom measurement.

Comparison of VFI in vivo and CFD

The CFD model for comparison with the VFI *in vivo* scan used an inlet condition constructed from a mean spatial velocity profile provided by the through-plane velocities from the MRA scan. Because of the different peak velocities for the CFD data and VFI *in vivo* scan, the velocity estimates in Figures 7 and 8 are normalized by the peak velocities (0.9 m/s for CFD and 0.7 m/s for VFI *in vivo*). A qualitative comparison of the flow fields is thereby provided. Figure 7 illustrates a frame from peak systole, where similar flow patterns were obtained, including the formation of a small vortex near the upper wall of the ICA. The location of the vortex was approximately the same as in the phantom measurement (see Fig. 2). However, the vortex was not as well defined in the CFD simulation as in the *in vivo* scan. Figure 8 illustrates the systolic deceleration,

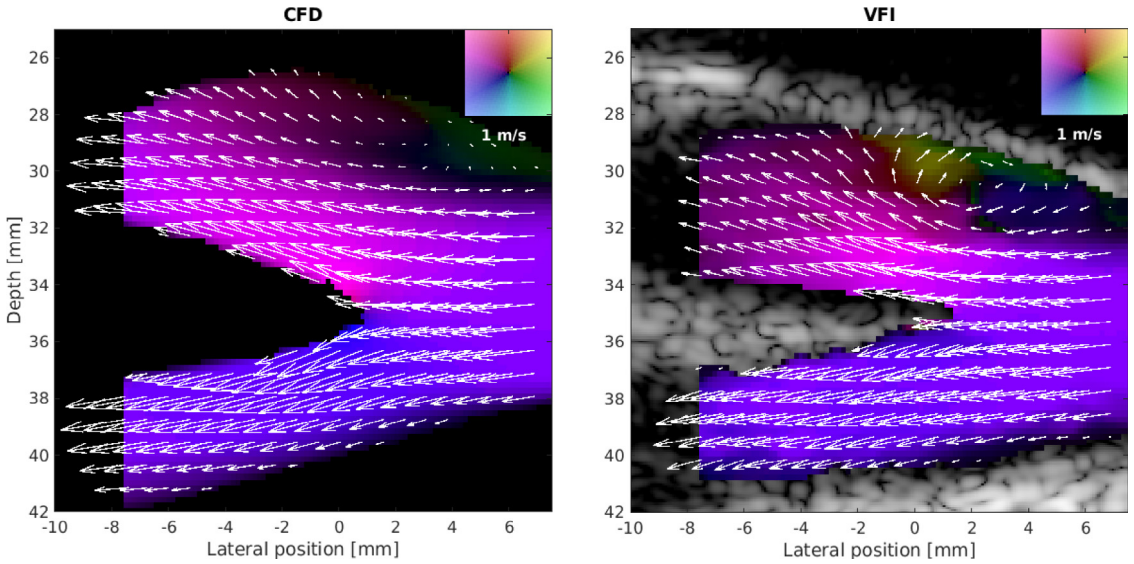

Fig. 7. Velocity estimates from CFD simulation (left) and VFI *in vivo* scan (right). The frame is from the peak systolic phase. CFD = computational fluid dynamics; VFI = vector flow imaging.

where different flow patterns were attained: The large recirculation zone in the ICA as predicted by CFD was not measured by VFI *in vivo*, whereas the opposite was obtained in the ECA.

Comparison of VFI, MRA and spectral Doppler

The PSVs for plane wave VFI were compared with MRA and spectral Doppler for the volunteers. Figure 9 is an example of through-plane velocities measured using MRA, where a PSV of 0.75 m/s is detected in the two CCAs (*red areas*) in one of the volunteers. A Bland–Altman plot of the PSVs for plane wave VFI versus MRA and plane wave VFI versus spectral Doppler is provided in Figure 10. The mean difference between plane wave VFI and MRA was –0.17 m/s, and the mean difference between plane wave VFI and spectral Doppler was 0.07 m/s. The highest PSV was 1.2 m/s. The difference between plane wave VFI and MRA was significant ($p = 0.002$), whereas there was no significant difference between plane wave VFI and spectral Doppler ($p = 0.19$). Linear regression between plane wave VFI and MRA yielded a correlation coefficient of 0.78, and that between plane wave VFI and spectral Doppler yielded a correlation coefficient of 0.70. MRA consistently estimated PSV

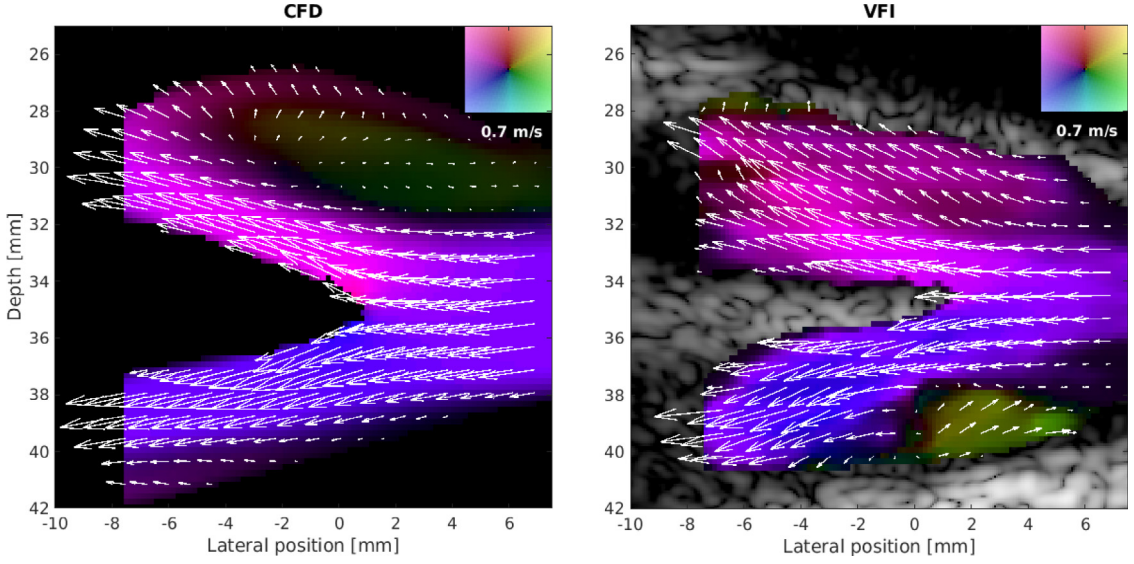

Fig. 8. Velocity estimates from CFD simulation (left) and VFI *in vivo* scan (right). The frame is within the systolic deceleration. CFD = computational fluid dynamics; VFI = vector flow imaging.

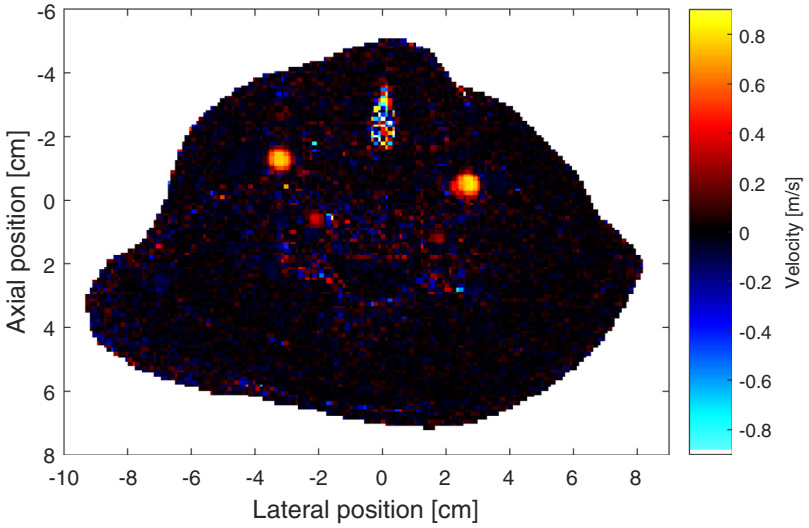

Fig. 9. Through-plane velocities measured using magnetic resonance angiography at peak systole. The selected plane covers the two common carotid arteries on the neck of one of the volunteers.

lower compared with plane wave VFI, and spectral Doppler estimated higher PSVs than plane wave VFI for all except 2 volunteers. It can also be noted that the differences between the methods were more pronounced for high PSVs than for low PSVs.

Precision of VFI in vivo

Figure 11 illustrates an example of velocity profiles and angles aligned according to the cardiac cycle. The data were from an evaluation point close to the vessel wall of the CCA. Initially, the SD of angles and velocities were calculated as a mean throughout the whole cardiac cycle automatically by the visualization program using eqn (2). However, the angle naturally fluctuated randomly when very low velocities were present, as illustrated in Figure 11. The angles were much more stable when higher-velocity flow was present. Data for the angles were therefore also analyzed for each volunteer by calculating the SD of the angles, when the velocity magnitude was above 10% of the temporal peak velocity at the evaluation point.

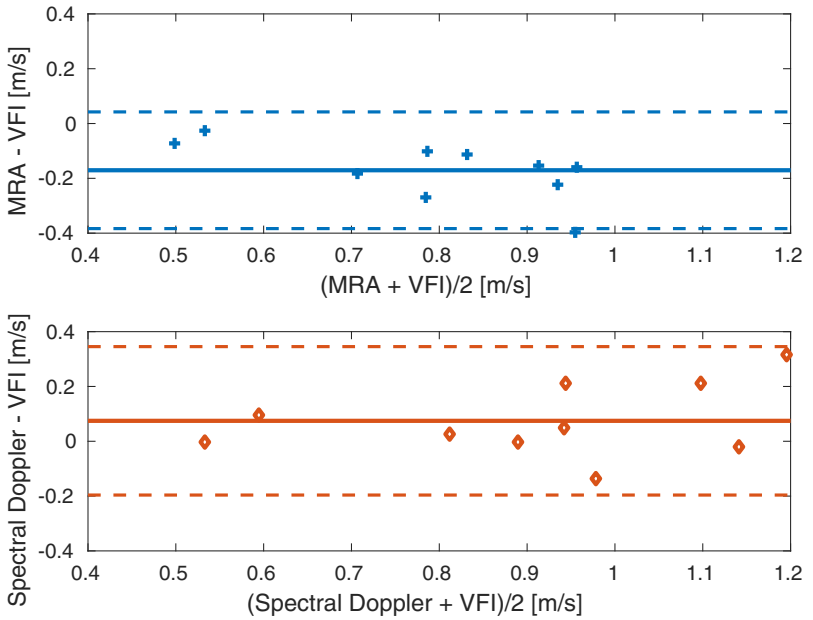

Fig. 10. Bland–Altman plot of PSVs for plane wave VFI compared with MRA (top) and spectral Doppler (bottom). *Solid lines* represents mean differences, and *dashed lines*, means ± 2 standard deviations. MRA = magnetic resonance angiography; PSV = peak systolic velocity; VFI = vector flow imaging.

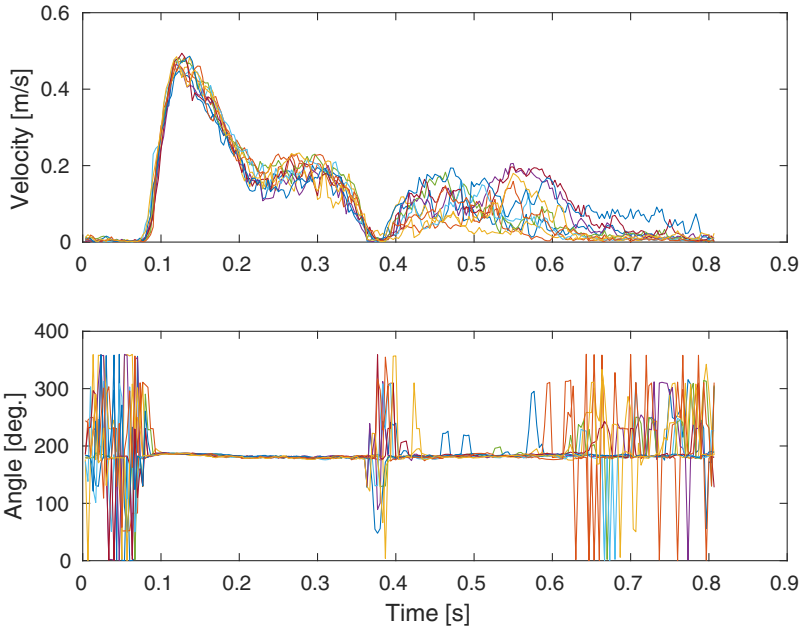

Fig. 11. Velocities (top) and angles (bottom) for volunteer 6 with the evaluation point close to the vessel wall. Estimates are aligned to the cardiac cycle, and each colored curve is for one cardiac cycle.

Figure 12 illustrates the evaluation for one of the volunteers. Evaluation points were selected in the ICA, close to the vessel wall of the CCA and in the center of the CCA. The velocity magnitude estimates at each point were aligned to the heart cycle. The vorticity inside the *blue box* is also shown, whereas the ECA was not visible on this scan.

The study provided results for the mean SD of velocity magnitude estimates and angles for each volunteer for evaluation points in the CCA and bulb scans. Table 2 summarizes the the median values and ranges of the volunteers. The results for angles were calculated throughout the whole cardiac cycle and for frames in which low-velocity flow was excluded (right column). High precision of the velocity magnitude was obtained in the center of the CCA with a median SD among the volunteers of 3.6%; a slightly lower precision was obtained near the CCA wall (6.8%). The angle estimates in the center of the CCA attained a precision of 4.8°. Near the vessel wall, the median SD among the volunteers increased to 31.7°, when using estimates throughout the

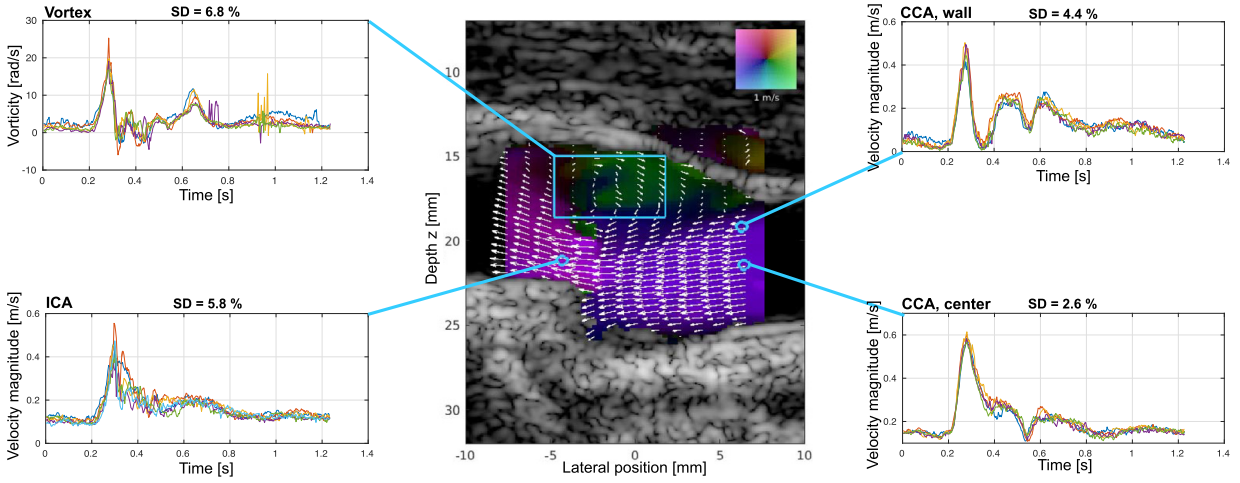

Fig. 12. Vector flow imaging of the carotid bulb for one of the volunteers. The frame is from the systole, where a large vortex was created in the bulb. The total vorticity within the *blue box* is plotted as a function of time at the top left. Velocity magnitudes are also depicted for evaluation points in the ICA, close to the vessel wall of the CCA and the center of the CCA. CCA = common carotid artery; ICA = internal carotid artery.

Table 2. Precision in terms of median standard deviation for the 10 volunteers using estimates of the velocity magnitude, angle and angle when excluding low flow*

Evaluation point	Velocity magnitude	Angle	Angle (excluding low flow)
CCA, center	3.6% (2.7%– 6.8%)	4.8° (1.2°– 25.7°)	4.5° (1.2°–20.3°)
CCA, wall	6.8% (2.9%–9.2%)	31.7° (6.3°–83.0°)	11.0° (1.2°–19.1°)
ICA	7.5% (5.4%–18.7%)	6.8° (2.0°–32.2°)	6.8° (2.0°–32.2°)
ECA	10.2% (5.1%–30.8%)	54.1° (5.1°–30.8°)	39.0° (8.3°–100.3°)

CCA = common carotid artery; ECA = external carotid artery; ICA = internal carotid artery.
* The precision was evaluated in the center of the CCA, close to the vessel wall of the CCA, in the ICA, and the ECA.

cardiac cycle. The median SD decreased to 11.0° when low-velocity flow was excluded.

For evaluation points in the CCA of the scans of the carotid bulb, the median SD of the velocity magnitudes was slightly higher than that for the CCA scans; for example, the median SD in the CCA center was 8.1% for the bulb scans. The SDs of the angle estimates were at about the same levels as those for the CCA scans.

Results for evaluation points in the ICA and ECA for the scans of the carotid bulb indicated a higher precision of velocity magnitude and angles in the ICA than in the ECA. The angles were estimated with a low precision in the ECA, where the median SD was 54.1°, when using estimates throughout the cardiac cycle. A small reduction in SD to 39.0° was obtained when excluding frames with low-velocity flow.

Vortices were present in 8 of 10 volunteers—some vortices were very small and rapidly formed and disappeared, whereas others filled most of the carotid sinus. Most vortices were present during or immediately after peak systole and developed in the low-velocity flow areas in the bulb. For the eight vortices, vorticity was estimated with a precision of 6.9% (range: 4.9%– 12.3%).

DISCUSSION

In this study, the accuracy and precision of a plane wave VFI method were investigated in the carotid arteries of healthy volunteers. CFD simulations of the velocity field were used with boundary conditions corresponding to the velocity variation in a flow phantom and *in vivo* to perform a qualitative and quantitative comparison with VFI measurements. Comparison between a CFD simulation and a VFI phantom measurement revealed that similar flow fields and velocity magnitudes were obtained throughout the bifurcation at the two times (Figs. 2–5). The RMS difference between CFD and VFI was lowest for v_z and in the range 0.023 m/s to 0.047 m/s. The RMS difference was larger for v_x and reached 0.17 m/s during systolic deceleration, when velocities were measured lower than in the CFD simulation. A large recirculation zone appeared in both the phantom measurement and simulation at the same time during systolic deceleration or slightly earlier in the measurement. This was also shown in Figure 6(b), where the vorticity showed good agreement between CFD simulation and VFI, except at the onset of the rotation at 0.15 s.

The impact of the applied echo-canceling filter on VFI estimates was investigated by Villagomez-Hoyos et al. (2017) in simulations, which indicated that the TO–DB method generally underestimated velocities, especially for fully transverse flow. This was due partly to remaining tissue signal after echo canceling and spectral leakage from the tissue signal. These factors may also have had an impact on the velocity estimates in the VFI scans in this study.

Previous studies have used simulated ultrasound images obtained with Field II to compare derived flow estimates with CFD-simulated velocities in carotid bifurcation geometries, in the forearm vasculature and in a neonatal heart model (Canneyt et al. 2013; Cauwenberge et al. 2016; Swillens et al. 2009). Simulations represent ideal situations, whereas measurements do not. Measurements are affected by noise in the ultrasound system and by imperfections of the transducer, phantom and flow pump. The phantom measurement resembled several conditions under an *in vivo* scan, but provided better control over the scan environment.

The alignment between transducer scan plane in the measurement and CFD-simulated velocities was not perfect. The ECA, in particular, appeared more narrow and/or slightly translated vertically. Furthermore, the phantom material had shrunk slightly during the time from initial fabrication to measurement, which may have affected the size of the vessels. A limitation of the CFD simulation was that the vessel walls were assumed to be rigid. However, the vessel walls of the fabricated phantom moved during systole (axial velocities of ±2 mm/s), which changed the flow pattern and may explain the differences in vortex development between measurement and CFD simulation. If vessel wall movement should be taken into account in the CFD simulation, fluid–structure interaction simulation models could be included (Swillens et al. 2010). This requires a much more complicated CFD model, which has yet to be developed. The CFD simulation should be considered an independent method against which to compare VFI, and not the ground truth, because CFD is based on

models and assumptions, which may not be entirely valid for the specific measurement. These include assumptions of the inlet and outlet boundary conditions, where the assumption of a pressure of 0 Pa at both outlets may not be valid physically, as the pressure fields in the ECA and ICA differ.

The comparison between a CFD simulation and a VFI scan *in vivo* revealed similar flow patterns at peak systole; however, different flow patterns and recirculation zones were obtained during systolic deceleration. Future work is anticipated to further develop CFD models for comparing CFD with VFI *in vivo* scans and to further investigate the difference in PSV, which was obtained for CFD and VFI *in vivo*.

Investigation of the accuracy of PSV for laminar flow in the CCA (Fig. 10) revealed a mean difference of −0.17 m/s between plane wave VFI and MRA. Previous studies have reported a negative bias when comparing MRA with spectral Doppler for flow in the carotid bifurcation (Harloff et al. 2013) and across the mitral valve (Karwatowski et al. 1995). The difference may be caused by the lower spatial and temporal resolution in MRA than in plane wave VFI. Data from VFI were averaged over about 10 cardiac cycles during the 10-s scan sequence, whereas MRA data were averaged over 210 cardiac cycles, which was effectively a low-pass filtering of the data. The mean difference between plane wave VFI and spectral Doppler was 0.07 m/s. It is known that spectral Doppler has a positive bias caused by spectral broadening, which was also reported for plane wave vector Doppler (Tortoli et al. 2015). In addition to spectral broadening, the performance of spectral estimators is affected by the manual determination of the beam-to-flow angle (Newhouse et al. 1980). Furthermore, the Bland–Altman plot in Figure 10 illustrated a larger difference in PSV for higher mean PSVs than low mean PSVs. This may be caused by transit time broadening of the Doppler spectrum, where blood moving at high velocities is observed for a shorter period within the US beam, which further broadens the spectrum (Jensen 1996). The plane wave VFI method was not affected by the same factors as spectral estimators, because received signals from emission to emission were directly correlated to find the time or phase shift between pulses. Thus, the angle independency and the use of a phase shift estimator for the plane wave VFI method may be advantageous compared with spectral Doppler, especially for the assessment of a carotid stenosis, where the flow angle is close to 90° and velocities reach ≥1 m/s.

Plane wave imaging can be combined with VFI methods other than the TO–DB method used in this study. It has been reported that TO–DB is superior to TO for low beam-to-flow angles, whereas TO–DB slightly underestimates velocities for flow transverse to the ultrasound beam (Jensen et al. 2017). Generally, the speckle tracking method has reduced performance for the lateral velocity estimate at low beam-to-flow angles (Udesen et al. 2008), and cross-beam methods are susceptible to velocity errors at large beam-to-flow angles (Fadnes et al. 2015).

The precision of the plane wave VFI method was investigated at several evaluation points in the vessels. The highest precision was found in the center of the CCA with laminar uni-directional flow (median SD = 3.6% for velocities and 4.8° for angles for the 10 volunteers). The precision was roughly a factor of 2 lower close to the vessel wall of the CCA compared with the center. For 6 volunteers, blood flow signals close to the vessel wall were dominated by tissue signal and/or noise remaining after echo canceling, which worsened the precision of the velocity estimates. The diameters of the ICA and ECA were smaller than that of the CCA, and the flow was multi-directional. This affected the precision of the velocities (median SD = 7.5% in the ICA and 10.2% in the ECA). The lowest precision for angles was found in the ECA with a mean SD of 39°, where the flow patterns were not exactly repeatable from one cardiac cycle to the next one. Vortices were characterized by calculating the vorticity, which exhibited a repeatable pattern between cardiac cycles, as the SD of the vorticity was 6.9%. Calculation of the total vorticity within a box covering a vortex reduced the SD of the estimates when compared with the single-point estimations listed in Table 2. The reliable estimation of vortices may also be of clinical interest: It has been speculated that the presence of a stable vortex in the carotid bulb is essential for blood pressure regulation, as the carotid bulb has a high concentration of baroreceptors (Hansen 2010). The complex flow patterns present in the carotid bulb have also been studied using 2-D echo particle image velocimetry by using the higher signal-to-noise ratio for microbubbles than red blood cells. When compared with optical particle image velocimetry in a flow phantom, good agreement was obtained qualitatively (Zhang et al. 2011). Velocities and wall shear stress were measured with high repeatability and reproducibility *in vivo* and with a mean difference of −10% when compared with MRA, which is similar to the results obtained in this study (Gurung et al. 2017). Imaging of an intracardiac vortex is also of interest for diagnosis of diastolic heart function, and the peak vorticity estimated using VFI has shown good agreement with MRA (Faurie et al. 2017).

The VFI phantom measurement of complex flow indicated that similar flow patterns were predicted by CFD, which strengthens the validity of using plane wave VFI to measure complex flow patterns. Phantoms with different degrees of stenosis could be considered in a future work, as the presence of a significant stenosis may create flow patterns, which affect the precision and accuracy of the VFI method. It would provide further insight into the performance of the method for complex flow quantification

in both healthy and diseased vessels. Velocities may reach 2–3 m/s in stenotic vessels. Theoretically, the TO–DB method should be able to detect these high velocities, if the length of the directional lines is increased accordingly and decorrelation effects are minimized using, for example, high frame rates. However, these effects will be present *in vivo* in addition to worse signal-to-noise ratio (SNR) conditions for patients with stenotic and deep vessels. The TO–DB method has been investigated under different SNR conditions (Jensen et al. 2017), and it was found that the transverse velocity estimates had the same performance as the axial component when the SNR was above 0 dB. Future phantom and *in vivo* studies in patients may reveal how the method performs under conditions with higher velocities and poor SNRs. A recent study found that a plane wave VFI method using tracking Doppler was feasible under such conditions (Avdal et al. 2017).

A validation of VFI methods *in vivo* is complicated, because there is no ground truth. Although this work suggested a validation setup consisting of a phantom measurement, CFD simulation, MRA scan, and *in vivo* ultrasound scans, it should be noted that these techniques have their own limitations and assumptions and are affected by their configurations. A standard setup was used for the techniques, but other configurations may have led to other differences between the techniques. However, the comparison of plane wave VFI with several state-of-the-art methods indicated relatively low differences, which is encouraging. This has to be confirmed in clinical studies that include larger populations with both healthy volunteers and patients with cardiovascular diseases. Large clinical studies may also reveal how vortices and other complex flow patterns can provide new information to the clinician. This has been indicated for patients with stenotic aortic valves (Hansen et al. 2017).

CONCLUSIONS

The study described here investigated the precision and accuracy of plane wave VFI in the carotid artery in 10 volunteers. The comparison between flow measured in a carotid bifurcation phantom using VFI and CFD velocities simulated in the same geometry revealed similar flow patterns including recirculation zones. The RMS difference between CFD and VFI for velocities were within 0.12 m/s in the CCA and ICA, but an RMS difference of 0.17 m/s was obtained in the ECA. Among the 10 volunteers, the precision *in vivo* was highest in the center of the CCA (SD = 3.6% for velocity magnitudes) and lowest in the ECA (SD = 10.2% for velocity magnitudes). The plane wave VFI method estimated the vorticity with a SD of 6.9%. The study indicated that plane wave VFI can yield angle-independent and quantitative estimates of both laminar and complex flow dynamics in the carotid artery, which may give the clinician a new tool for assessing the health of blood vessels.

Acknowledgments—This work was supported by Grant 82-2012-4 from the Danish National Advanced Technology Foundation and by BK Ultrasound Aps, Herlev, Denmark.

SUPPLEMENTARY DATA

Supplementary data related to this article can be found at https://doi.org/10.1016/j.ultrasmedbio.2018.03.017.

REFERENCES

Anderson ME. Multi-dimensional velocity estimation with ultrasound using spatial quadrature. IEEE Trans Ultrason Ferroelectr Freq Control 1998;45:852–861.

Avdal J, Løvstakken L, Torp H, Ekroll IK. Combined 2-D vector velocity imaging and tracking Doppler for improved vascular blood velocity quantification. IEEE Trans Ultrason Ferroelectr Freq Control 2017;64:1795–1804.

Bamford J, Sandercock P, Dennis M, Burn J, Warlow C. Classification and natural history of clinically identifiable subtypes of cerebral infarction. Lancet 1991;337:1521–1526.

Bercoff J, Montaldo G, Loupas T, Savery D, Meziere F, Fink M, Tanter M. Ultrafast compound Doppler imaging: Providing full blood flow characterization. IEEE Trans Ultrason Ferroelectr Freq Control 2011; 58:134–147.

Canneyt KV, Swillens A, Løvstakken L, Antiga L, Verdonck P, Segers P. The accuracy of ultrasound volume flow measurements in the complex flow setting of a forearm vascular access. J Vasc Access 2013;14:281–290.

Cauwenberge JV, Lovstakken L, Fadnes S, Rodriguez-Morales A, Vierendeels J, Segers P, Swillens A. Assessing the performance of ultrafast vector flow imaging in the neonatal heart via multiphysics modeling and in vitro experiments. IEEE Trans Ultrason Ferroelectr Freq Control 2016;63:1772–1785.

Cebral J, Yim P, Lohner R, Soto O, Choyke P. Blood flow modeling in carotid arteries with computational fluid dynamics and MR imaging. Acad Radiol 2002;9:1286–1299.

Corriveau M, Johnston K. Interobserver variability of carotid Doppler peak velocity measurements among technologists in an ICAVL-accredited vascular laboratory. J Vasc Surg 2004;39:735–741.

Dunmire B, Beach KW, Labs KH, Plett M, Strandness DE. Cross-beam vector Doppler ultrasound for angle independent velocity measurements. Ultrasound Med Biol 2000;26:1213–1235.

Ekroll IK, Swillens A, Segers P, Dahl T, Torp H, Lovstakken L. Simultaneous quantification of flow and tissue velocities based on multi-angle plane wave imaging. IEEE Trans Ultrason Ferroelectr Freq Control 2013;60:727–738.

Ekroll IK, Dahl T, Torp H, Løvstakken L. Combined vector velocity and spectral Doppler imaging for improved imaging of complex blood flow in the carotid arteries. Ultrasound Med Biol 2014;40:1629–1640.

Evans DH. Some aspects of the relationship between instantaneous volumetric blood flow and continuous wave Doppler ultrasound recordings: III. The calculation of Doppler power spectra from mean velocity waveforms, and the results of processing these spectra with maximum, mean, and RMS frequency processors. Ultrasound Med Biol 1982;8:617–623.

Fadnes S, Ekroll IK, Nyrnes SA, Torp H, Løvstakken L. Robust angle-independent blood velocity estimation based on dual-angle plane wave imaging. IEEE Trans Ultrason Ferroelectr Freq Control 2015;62: 1757–1767.

Faurie J, Baudet M, Assi KC, Auger D, Gilbert G, Tournoux F, Garcia D. Intracardiac vortex dynamics by high-frame-rate doppler vortography—In vivo comparison with vector flow mapping and 4-D

flow MRI. IEEE Trans Ultrason Ferroelectr Freq Control 2017;64: 424–432.
Fox MD. Multiple crossed-beam ultrasound Doppler velocimetry. IEEE Trans Son Ultrason 1978;SU-25:281–286.
Gurung A, Gates PE, Mazzaro L, Fulford J, Zhang F, Barker AJ, Hertzberg J, Aizawa K, Strain WD, Elyas S, Shore AC, Shandas R. Echo particle image velocimetry for estimation of carotid artery wall shear stress: Repeatability, reproducibility and comparison with phase-contrast magnetic resonance imaging. Ultrasound Med Biol 2017; 43:1618–1627.
Hansen KL. In-vivo studies of new vector velocity and adaptive spectral estimators in medical ultrasound. Dan Med Bull 2010;57:1–23.
Hansen KL, Udesen J, Gran F, Jensen JA, Nielsen MB. In-vivo examples of flow patterns with the fast vector velocity ultrasound method. Ultraschall Med 2009a;30:471–476.
Hansen KL, Udesen J, Oddershede N, Henze L, Thomsen C, Jensen JA, Nielsen MB. In vivo comparison of three ultrasound vector velocity techniques to MR phase contrast angiography. Ultrasonics 2009b; 49:659–667.
Hansen KL, Møller-Sørensen H, Kjaergaard J, Jensen MB, Jensen JA, Nielsen MB. Aortic valve stenosis increases helical flow and flow complexity: A study of intra-operative cardiac vector flow imaging. Ultrasound Med Biol 2017;43:1607–1617.
Harloff A, Zech T, Wegent F, Strecker C, Weiller C, Markl M. Comparison of blood flow velocity quantification by 4D flow MR imaging with ultrasound at the carotid bifurcation. AJNR Am J Neuroradiol 2013;34:1407–1413.
Holbek S, Ewertsen C, Bouzari H, Pihl MJ, Hansen KL, Stuart MB, Nielsen MB, Jensen JA. Ultrasonic 3-D vector flow method for quantitative in vivo peak velocity and flow rate estimation. IEEE Trans Ultrason Ferroelectr Freq Control 2017;64:544–554.
Jensen J, Villagomez-Hoyos CA, Stuart MB, Ewertsen C, Nielsen MB, Jensen JA. Fast plane wave 2-D vector flow imaging using transverse oscillation and directional beamforming. IEEE Trans Ultrason Ferroelectr Freq Control 2017;64:1050–1062.
Jensen JA. Estimation of blood velocities using ultrasound: A signal processing approach. New York: Cambridge University Press; 1996.
Jensen JA. Directional velocity estimation using focusing along the flow direction: I. Theory and simulation. IEEE Trans Ultrason Ferroelectr Freq Control 2003;50:857–872.
Jensen JA, Munk P. A new method for estimation of velocity vectors. IEEE Trans Ultrason Ferroelectr Freq Control 1998;45:837–851.
Jensen JA, Holten-Lund H, Nilsson RT, Hansen M, Larsen UD, Domsten RP, Tomov BG, Stuart MB, Nikolov SI, Pihl MJ, Du Y, Rasmussen JH, Rasmussen MF. SARUS: A synthetic aperture real-time ultrasound system. IEEE Trans Ultrason Ferroelectr Freq Control 2013; 60:1838–1852.
Karwatowski SP, Brecker SJD, Yang GZ, Firmin DN, Sutton MSJ, Underwood SR. Mitral valve flow measured with cine MR velocity mapping in patients with ischemic heart disease: Comparison with Doppler echocardiography. J Magn Reson Imaging 1995;5:89–92.
Kruskal JB, Newman PA, Sammons LG, Kane RA. Optimizing Doppler and color flow US: Application to hepatic sonography. Radiographics 2004;24:657–675.
Lai SSM, Yiu BYS, Poon AKK, Yu ACH. Design of anthropomorphic flow phantoms based on rapid prototyping of compliant vessel geometries. Ultrasound Med Biol 2013;39:1654–1664.
Lenge M, Ramalli A, Tortoli P, Cachard C, Liebgott H. Plane-wave transverse oscillation for high-frame-rate 2-D vector flow imaging. IEEE Trans Ultrason Ferroelectr Freq Control 2015;62:2126–2137.
Lotz J, Meier C, Leppert A, Galanski M. Cardiovascular flow measurement with phase-contrast MR imaging: Basic facts and implementation. Radiographics 2002;22:651–671.
Lui E, Steinman A, Cobbold R, Johnston K. Human factors as a source of error in peak Doppler velocity measurement. J Vasc Surg 2005; 42:972–979.
Naghavi M, Libby P, Falk E, Casscells SW, Litovsky S, Rumberger J, Badimon JJ, Stefanadis C, Moreno P, Pasterkamp G, Fayad Z, Stone PH, Zipes DP, Shah PK, Willerson JT. From vulnerable plaque to vulnerable patient: A call for new definitions and risk assessment strategies: Part 1. Circulation 2003;108:1664–1672.
Newhouse VL, Furgason ES, Johnson GF, Wolf DA. The dependence of ultrasound Doppler bandwidth on beam geometry. IEEE Trans Son Ultrason 1980;SU-27:50–59.
Newhouse VL, Censor D, Vontz T, Cisneros JA, Goldberg BB. Ultrasound Doppler probing of flows transverse with respect to beam axis. IEEE Trans Biomed Eng 1987;BME-34:779–788.
Nikolov SI, Jensen JA. In-vivo synthetic aperture flow imaging in medical ultrasound. IEEE Trans Ultrason Ferroelectr Freq Control 2003;50: 848–856.
Pedersen MM, Pihl MJ, Hansen JM, Hansen PM, Haugaard P, Nielsen MB, Jensen JA. Secondary arterial blood flow patterns visualised with vector flow ultrasound. Proc IEEE Ultrason Symp 2011;1242–1245.
Pedersen MM, Pihl MJ, Haugaard P, Hansen KL, Lange T, Lonn L, Nielsen MB, Jensen JA. Novel flow quantification of the carotid bulb and the common carotid artery with vector flow ultrasound. Ultrasound Med Biol 2014;40:2700–2706.
Salles S, Chee AJY, Garcia D, Yu ACH, Vray D, Liebgott H. 2-D arterial wall motion imaging using ultrafast ultrasound and transverse oscillations. IEEE Trans Ultrason Ferroelectr Freq Control 2015; 62:1047–1058.
Steinman D, Poepping T, Tambasco M, Rankin R, Holdsworth D. Flow patterns at the stenosed carotid bifurcation: Effect of concentric versus eccentric stenosis. Ann Biomed Eng 2000;28:415–423.
Stewart SFC. Effects of transducer, velocity, doppler angle, and instrument settings on the accuracy of color Doppler ultrasound. Ultrasound Med Biol 2001;27:551–564.
Swillens A, Løvstakken L, Kips J, Torp H, Segers P. Ultrasound simulation of complex flow velocity fields based on computational fluid dynamics. IEEE Trans Ultrason Ferroelectr Freq Control 2009;56: 546–556.
Swillens A, Degroote J, Vierendeels J, Løvstakken L, Segers P. A simulation environment for validating ultrasonic blood flow and vessel wall imaging based on fluid–structure interaction simulations: Ultrasonic assessment of arterial distension and wall shear rate. Med Phys 2010;37:4318–4330.
Tortoli P, Bambi G, Ricci S. Accurate Doppler angle estimation for vector flow measurements. IEEE Trans Ultrason Ferroelectr Freq Control 2006;53:1425–1431.
Tortoli P, Lenge M, Righi D, Ciuti G, Liebgott H, Ricci S. Comparison of carotid artery blood velocity measurements by vector and standard Doppler approaches. Ultrasound Med Biol 2015;41:1354–1362.
Trahey GE, Allison JW, von Ramm OT. Angle independent ultrasonic detection of blood flow. IEEE Trans Biomed Eng 1987;BME-34: 965–967.
Udesen J, Gran F, Hansen KL, Jensen JA, Thomsen C, Nielsen MB. High frame-rate blood vector velocity imaging using plane waves: Simulations and preliminary experiments. IEEE Trans Ultrason Ferroelectr Freq Control 2008;55:1729–1743.
U.S. Food and Drug Administration (FDA). Information for manufacturers seeking marketing clearance of diagnostic ultrasound systems and transducers. Technical report. Silver Spring, MD: Center for Devices and Radiological Health, U.S. FDA, 2008.
Villagomez-Hoyos CA, Jensen J, Ewertsen C, Hansen KL, Nielsen MB, Jensen JA. Energy based clutter filtering for vector flow imaging. Proc IEEE Int Ultrason Symp 2017:1–4.
Womersley JR. Oscillatory motion of a viscous liquid in a thin-walled elastic tube: I. The linear approximation for long waves. Phil Mag 1955;46:199–221.
Yiu BY, Lai SS, Yu AC. Vector projectile imaging: Time-resolved dynamic visualization of complex flow patterns. Ultrasound Med Biol 2014; 40:2295–2309.
Zhang F, Lanning C, Mazzaro L, Barker AJ, Gates PE, Strain WD, Fulford J, Gosling OE, Shore AC, Bellenger NG, Rech B, Chen J, Chen J, Shandas R. In vitro and preliminary in vivo validation of echo particle image velocimetry in carotid vascular imaging. Ultrasound Med Biol 2011;37:450–464.